arXiv:1510.03355v2 [cond-mat.quant-gas] 10 Nov 2015

Dirac and Weyl Rings in Three Dimensional Cold Atom Optical Lattices

Yong Xu and Chuanwei Zhang*
Department of Physics, University of Texas at Dallas, Richardson, Texas 75080, USA

Recently three dimensional topological quantum materials with gapless energy spectra have attracted considerable interests in many branches of physics. Besides the celebrated example, Dirac and Weyl points which possess gapless point structures in the underlying energy dispersion, the topologically protected gapless spectrum can also occur along a ring, named Dirac and Weyl nodal rings. Ultra-cold atomic gases provide an ideal platform for exploring new topological materials with designed symmetries. However, whether Dirac and Weyl rings can exist in the single-particle spectrum of cold atoms remains elusive. Here we propose a realistic model for realizing Dirac and Weyl rings in the single-particle band dispersion of a cold atom optical lattice. Our scheme is based on previously experimentally already implemented Raman coupling setup for realizing spin-orbit coupling. Without the Zeeman field, the model preserves both pseudo-time-reversal and inversion symmetries, allowing Dirac rings. The Dirac rings split into Weyl rings with a Zeeman field that breaks the pseudo-time-reversal symmetry. We examine the superfluidity of attractive Fermi gases in this model and also find Dirac and Weyl rings in the quasiparticle spectrum.

The topology of band structures plays a crucial role in many important phenomena [1–4] in various physical fields, ranging from solid-state materials to photonic crystals, and to cold atomic gases. Remarkably, apart from gapped topological insulators that exhibit metallic edge states protected by symmetries [3, 4], materials with gapless band dispersions could also possess non-trivial topological properties and protected edge states. A well-known example of two-dimensional gapless materials is graphene with Dirac points [2]. In recent years, gapless Dirac and Weyl points in three dimensions (3D) have been theoretically predicted [5–12] and experimentally observed [13–18] in a variety of Dirac and Weyl semimetals. Besides isolated topological gapless points, the gaps of energy spectra in 3D could also close along a line, forming Dirac and Weyl nodal rings in nodal semimetals [19–28]. The dispersion of the surface states in these nodal semimetals vanishes, suggesting a potential type of high temperature superconductivity [29].

Cold atomic gases provide a clean platform for discovering new topological quantum materials due to their high controllability for engineering Hamiltonians with desired symmetries and versatile tools for directly probing topological states. In this context, recent experimental achievements for realizing cold atom topological matter, both gapped and gapless, mainly focus on low dimensional (2D or 1D) systems, including the realization of topological Haldane model [30] for quantum anomalous quantum Hall effects, the observation of Zak phase [31] and topological charge pumping in optical superlattices [32–34], the realization of Dirac cones in optical lattices [35] and spin-orbit-coupled gases [36]. In 3D, however, various topological gapless structures such as Weyl points, structured Weyl points, Weyl rings, and structured Weyl rings have only been theoretically predicted in the quasiparticle spectrum of superfluids [37–44]. One exception is the Weyl points that have been proposed in the single-particle spectrum of moving lattices [45, 46]. However, a realistic scheme for realizing Dirac and Weyl rings in the single-particle spectrum of cold atoms is still lacking and their corresponding superfluid properties have been unexplored.

In this paper, we propose an experimental scheme for engineering a Hamiltonian that hosts gapless Dirac or Weyl rings in its single-particle spectrum of cold atoms. The scheme is based on the experimentally already implemented Raman coupling setup for spin-orbit coupling [47–52], and therefore should be experimentally feasible. Our main results are:

(i) We construct a new spin-dependent Hamiltonian in the continuous space and derive its tight-binding form. Such Hamiltonian has not been discussed previously in solid-state materials [19–27]. The Hamiltonian preserves both pseudo-time-reversal and inversion symmetries without Zeeman fields, allowing the existence of Dirac rings. The pseudo-time-reversal symmetry is broken with a Zeeman field and a Dirac ring splits into two Weyl rings. The parameter regions as well as the topological characterization (e.g., topological invariance, surface states) for these topological gapless rings are obtained.

(ii) We investigate the superfluidity of attractive Fermi gases in this Hamiltonian and find two distinct superfluid phases (SF1 and SF2). The transition between them is the first order. Interestingly, Dirac and Weyl rings also exist in the quasiparticle spectra in certain region of the superfluid.

(iii) The spin-dependent Hamiltonian can be realized using an experimental setup based on previous Raman coupling scheme for spin-orbit coupling [47–52]. Specifically, two pairs of Raman laser beams are used to couple two hyperfine spin states of atoms for generating a specific spin-dependent optical lattice, which is essential for the creation of these topological nodal rings.

Model Hamiltonian: We start from a spin-dependent Hamiltonian in the continuous space that can support

the existence of nodal rings

$$H = \frac{\mathbf{p}^2}{2m} - \sum_{\nu=x,y,z} V_\nu \cos^2(k_{L\nu} r_\nu) + h_z\sigma_z - V_{SO}\sigma_y, \quad (1)$$

where $\mathbf{p} = -i\hbar\nabla$ is the momentum operator, m is the mass of atoms, V_ν and $a_\nu = \pi/k_{L\nu}$ are, respectively, the strength and period of a periodic lattice along the ν direction, h_z is the Zeeman field, σ_ν are Pauli matrices for spins, and $V_{SO} = \Omega_{SO}\sin(k_{Lx}r_x)\cos(k_{Ly}r_y)\cos(k_{Lz}r_z)$ corresponds to a spin-dependent optical lattice. For simplicity, we explore the physics of this Hamiltonian in the tight-binding model (see the supplementary information for its derivation and comparison with the continuous model) that can be written as

$$H_{TB} = H_h + H_Z + H_{SO}, \quad (2)$$

where $H_h = -\sum_j\sum_\sigma\sum_\nu(t_\nu\hat{c}^\dagger_{j,\sigma}\hat{c}_{j_\nu+1,\sigma} + t_{N\nu}\hat{c}^\dagger_{j,\sigma}\hat{c}_{j_\nu+2,\sigma} + h.c.)$ includes the nearest-neighbor (NN) and next nearest-neighbor (NNN) hopping with the tunneling amplitudes t_ν and $t_{N\nu}$, respectively, $H_Z = h_z\sum_j(\hat{c}^\dagger_{j,\uparrow}\hat{c}_{j,\uparrow} - \hat{c}^\dagger_{j,\downarrow}\hat{c}_{j,\downarrow})$ is the Zeeman field term, and $H_{SO} = it_{\rm SO}\sum_j(-1)^{j_x+j_y+j_z}(\hat{c}^\dagger_{j,\uparrow}\hat{c}_{j_x+1,\downarrow} - \hat{c}^\dagger_{j,\uparrow}\hat{c}_{j_x-1,\downarrow}) + h.c.$ is the position-dependent spin-orbit coupling term with the strength $t_{\rm SO}$. Here $\hat{c}^\dagger_{j,\sigma}$ ($\hat{c}_{j,\sigma}$) creates (annihilates) an atom at site j with spin σ.

The position dependent spin-orbit coupling of the Hamiltonian breaks the one site translation symmetry, leading to a unit cell consisting of two sites: A and B. These new unit cells form a rocksalt crystal structure as shown in Fig. 1(a). In the new basis $\Psi(\mathbf{k})^T$ with $\Psi(\mathbf{k}) = (\, e^{ik_xa_x}\hat{A}_{\mathbf{k}\uparrow}\ e^{ik_xa_x}\hat{A}_{\mathbf{k}\downarrow}\ \hat{B}_{\mathbf{k}\uparrow}\ \hat{B}_{\mathbf{k}\downarrow}\,)$, the Hamiltonian in the momentum space takes the form

$$H(\mathbf{k}) = h_{Nt} - h_t\tau_x + h_z\sigma_z + d_x\tau_y\otimes\sigma_y, \quad (3)$$

where $h_{Nt} = -2\sum_\nu t_{N\nu}\cos(2k_\nu a_\nu)$, $h_t = 2\sum_\nu t_\nu\cos(k_\nu a_\nu)$ and $d_x = 2t_{SO}\sin(k_xa_x)$. τ are Pauli matrices for the A, B sublattice space. In the absence of Zeeman fields ($h_z = 0$), this Hamiltonian preserves both the pseudo-time-reversal symmetry $\mathcal{T}^{-1}H\mathcal{T} = H(-\mathbf{k})$ with $\mathcal{T} = i\tau_x\otimes\sigma_y\mathcal{K}$ [53] and $\mathcal{K}$ being the complex conjugate operator, and the inversion symmetry $\mathcal{I}^{-1}H\mathcal{I} = H(-\mathbf{k})$ with $\mathcal{I} = \tau_x$. These two symmetries guarantee that the state at each $\mathbf{k}$ is at least two-fold degenerate, which implies that a gapless touching point, if exists, is four-fold degenerate. Therefore a ring formed by such gapless points is a Dirac ring. When one of the symmetries is broken, for instance, h_z breaks the pseudo-time-reversal symmetry, a Dirac ring splits into two Weyl rings, as visualized in Fig. 1(b).

The emergence of Dirac and Weyl rings can be seen from the energy spectrum of $H(\mathbf{k})$: $E_\lambda = h_{Nt} \pm \sqrt{(h_z+\lambda h_t)^2 + d_x^2}$ with $\lambda = \pm$. When $d_x = 0$ and $h_z + \lambda h_t = 0$, two bands (four bands when $h_z = 0$) touch

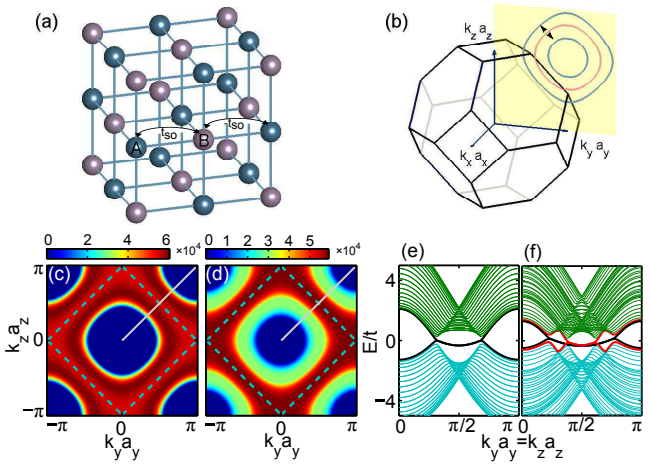

FIG. 1. (Color online) Lattice structure, Brillouin zone, and surface states. (a) and (b) Rocksalt lattice structure and corresponding first Brillouin zone. Dirac ($h_z = 0$) and Weyl rings ($h_z = 0.5t$), denoted by the red and blue rings respectively, are located at the $k_x = 0$ plane (yellow plane) around $(k_ya_y = \pi, k_za_z = \pi)$. (c) and (d) Without and with h_z, density of states at zero energy without including NNN hopping when there are edges along x. The dashed square indicates the first Brillouin zone. (e) and (f) Spectra along $k_ya_y = k_za_z$ [the grey line in (c) and (d)] with edges along x in the presence of NNN hopping, where the black and red lines denote the surface states. $t_x = 1.17t$, $t_y = t_z = t$, $t_{SO} = 0.53t$, and $t_N = -0.07t$. $a_x = a_y = a_z$.

to form nodal rings in the $\mathbf{k}$ space. In particular, for $-2t_1 < h_z < 2t_2$ or $-2t_2 < h_z < 2t_1$ with $t_1 = t_y + t_z + t_x$ and $t_2 = t_y + t_z - t_x$, such rings emerge in the $k_x = 0$ plane as shown in Fig. 1(b) (the rings in other planes can be obtained by translating the rings in this plane by a reciprocal vector). Clearly, when $h_z = 0$ and $t_y + t_z > t_x$, a four-fold degenerate Dirac ring appears. With h_z, the Dirac ring splits into Weyl rings, whose number equals to the number of the above conditions satisfied. Around a point on a nodal ring, the energy dispersion is linear except along the tangent direction to the ring. At the critical points (i.e., $h_z = \pm 2t_1, \pm 2t_2$), a ring shrinks to a point around which the dispersion is quadratic.

To discuss the topology of these nodal rings, we transform the tight-binding Hamiltonian (2) by $(-1)^{j_x+j_y+j_z}\hat{c}_{j,\uparrow} \to \hat{c}_{j,\uparrow}$ [54], which transforms Eq. (3) to

$$H_1(\mathbf{k}) = h_{Nt} + d_z\sigma_z - d_x\sigma_x, \quad (4)$$

with $d_z = h_t + h_z$. The eigenvalues are $E^\pm_{\mathbf{k}} = h_{Nt} \pm \sqrt{d_x^2 + d_z^2}$, where $\pm$ refer to the helicity, the eigenvalue of $H_1(\mathbf{k})/\sqrt{d_x^2+d_z^2}$.

This transformation simplifies the lattice structure to a simple cubic and hence enlarges the Brillouin zone so that one nodal ring in the $k_x = 0$ plane is moved to the $k_xa_x = \pi$ plane. In this transformed model that possesses the chiral symmetry, i.e., $\sigma_yH(\mathbf{k})\sigma_y = -H(\mathbf{k})$ in

the absence of NNN hoppings, we see that the Weyl ring can be characterized by the winding number $n_w = 1$ [55], the number of rotations that the vector $\mathbf{d} = d_z\mathbf{e}_x - d_x\mathbf{e}_y$ undergoes when it travels along a closed trajectory enclosing any gap closing point. Such nonzero n_w also amounts to the quantized Berry phase C_1 mod $2\pi = \pi$, half of the solid angle that $\mathbf{d}$ winds [56]. For a Dirac ring, the Hamiltonian (3) ($h_z = 0$) respects a σ_y symmetry, i.e., $\sigma_y H(\mathbf{k})\sigma_y = H(\mathbf{k})$, and hence each band in two subspaces with different eigenvalues $\sigma_y = \pm 1$ has a quantized Berry phase [57, 58]. We note that although the NNN hopping breaks the chiral symmetry by changing the eigenvalues, it does not modify the eigenstates, thereby leaving the quantized Berry phase unchanged.

In Fig. 1(c) and (d), we plot the surface density of states at zero energy (without NNN hoppings) when the edges are imposed along the x direction in the model (2). The density of states is extremely large between rings in different Brillouin zones, implying the vanishing dispersion of the surface states (i.e., the surface spectrum is flat). In the presence of NNN hoppings, the surface spectrum gains a slight dispersion as shown in Fig. 1(e) and (f) where the black and red lines denote the surface spectra. Without h_z, the surface spectra are four-fold degenerate, whereas with h_z, this four-fold degeneracy is lifted so that the surface states connecting different pairs of gapless points are separated (black and red lines). This breaking is also reflected in Fig. 1(d) where the density of states in the red region is twice as large as that in the green one.

Superfluids in nodal ring lattices: The Dirac and Weyl nodal ring lattices can be realized for both Bose and Fermi atoms. Here we consider fermionic cold atoms with contact attractive interactions that can be tuned by Feshbach resonances. With attractive interactions, Fermi gases form superfluids. Under the mean-field approximation, we can define the order parameter for both A and B sublattices, respectively, as $\Delta_A = -U\langle\hat{A}_{j\downarrow}\hat{A}_{j\uparrow}\rangle$ and $\Delta_B = -U\langle\hat{B}_{j\downarrow}\hat{B}_{j\uparrow}\rangle$ with the interaction strength U ($U > 0$). The dynamics of the superfluid is governed by the Bogliubov-de Gennes (BdG) Hamiltonian

$$H_{\rm BdG} = -\tau_{N,z}\otimes(h_t\tau_x+\tilde{\mu})+d_x\tau_y\otimes\sigma_y+h_z\sigma_z+H_{\rm BCS}, \quad (5)$$

where $\tilde{\mu} = \mu - h_{Nt}$ with the chemical potential μ, and τ_N act on the Nambu particle-hole space. This Hamiltonian is written in the Nambu basis $(\ \Psi(\mathbf{k})\ \ \tilde{\Psi}(\mathbf{k})\ )^T$ with $\tilde{\Psi}(\mathbf{k}) = (\ e^{ik_xa_x}\hat{A}^\dagger_{-\mathbf{k}\downarrow}\ \ -e^{ik_xa_x}\hat{A}^\dagger_{-\mathbf{k}\uparrow}\ \ \hat{B}^\dagger_{-\mathbf{k}\downarrow}\ \ -\hat{B}^\dagger_{-\mathbf{k}\uparrow}\ )$. Δ_A and Δ_B are obtained by numerically solving the nonlinear gap equations, see Methods.

Before we show the numerical results of Δ_A and Δ_B, we first analyze the conditions under which Dirac and Weyl rings can emerge in the quasiparticle spectrum. Our numerical results show that real Δ_A and Δ_B with $\Delta_A = |\Delta_B|$ are energetically preferred, therefore we only need to consider two superfluids phases: $\Delta_A = \Delta_B$ (dubbed SF1) and $\Delta_A = -\Delta_B$ (dubbed SF2), associated with $H_{BCS} = \Delta_A\tau_{N,x}$ and $H_{BCS} = \Delta_A\tau_{N,x}\otimes\tau_z$, respectively. When $h_z = 0$, both phases preserve the pseudo-time-reversal and inversion symmetries (see Methods), which guarantee that the quasiparticle spectra are at least two-fold degenerate at each $\mathbf{k}$. Therefore gapless rings, if exist, are four-fold degenerate Dirac rings because of these two symmetries and the intrinsic particle-hole symmetry. Finite h_z breaks the pseudo-time-reversal symmetry and splits the Dirac ring into two two-fold degenerate Weyl rings.

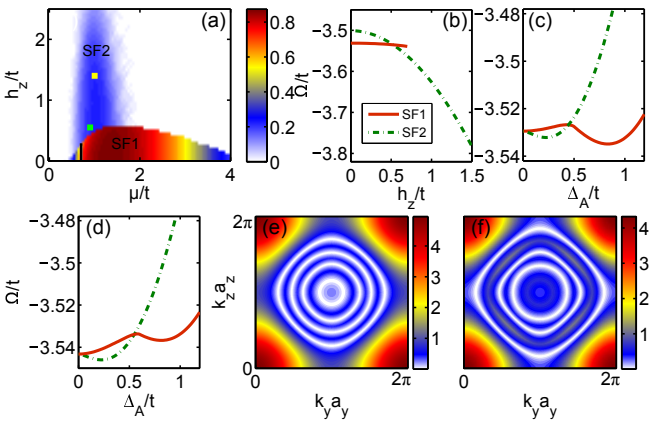

FIG. 2. (Color online) Phase diagram, thermodynamical potential, and the gap distribution. (a) The order parameter Δ_A as a function of μ and h_z at zero temperature. SF1 and SF2 correspond to the phases with $\Delta_A = \Delta_B$ and $\Delta_A = -\Delta_B$, respectively. A black line divides SF1 phase into gapless (left part) and gapped (right part) regions, while the whole SF2 phase is gapless. (b) The thermodynamical potential Ω of the SF1 (solid red line) and SF2 (dotted-dashed green line) phases with respect to h_z with $\mu = 1.1t$. Note that when $h_z > 0.7t$ the SF1 state is no longer an energy minimum state, while the SF2 state is in the whole region. (c) and (d) Ω as a function of Δ_A for the SF1 (solid red line) and SF2 (dotted-dashed line) for $\mu = 1.1t, h_z = 0.5t$ and $\mu = 1.1t, h_z = 0.6t$, respectively. (e) and (f) The gap of the quasiparticle spectrum with respect to k_ya_y and k_za_z in the $k_x = 0$ plane for the parameters denoted by the green and yellow squares in (a), respectively. Here $t_x = 1.17t$, $t_y = t_z = t$, $t_{SO} = 0.53t$, $t_N = -0.07t$, and $U = -4t$. $a_x = a_y = a_z$.

Specifically, for the SF1 state, in the absence of h_z, the eigenvalues of $H_{\rm BdG}$ are $E^\lambda_{\mathbf{k}\pm} = \pm\sqrt{h_0^2 + h_t^2 + d_x^2 + 2\lambda\sqrt{\tilde{\mu}^2h_t^2 + h_0^2d_x^2}}$ with $h_0^2 = \Delta_A^2 + \tilde{\mu}^2$ and $\lambda = \pm$. Each spectrum is two-fold degenerate. From $(E^+_{\mathbf{k}+})^2(E^-_{\mathbf{k}+})^2 = (h_0^2 - h_t^2 - d_x^2)^2 + 4\Delta_A^2h_t^2$, we see that $h_t = 0$ and $d_x^2 = h_0^2$ for gapless rings. The latter condition requires $\mu^2 \le 4t_{SO}^2 - \Delta_A^2$, if NNN hoppings are neglected. For the SF2 state, $E^{\lambda\nu}_{\mathbf{k}\pm} = \pm\sqrt{h_0^2 + (h_z + \nu h_t)^2 + d_x^2 + 2\lambda\sqrt{h_0^2(h_z + \nu h_t)^2 + \tilde{\mu}^2d_x^2}}$ with $\nu = \pm$. When $h_z = 0$, the spectra are two-fold degenerate, and this degeneracy is explicitly broken by h_z. Still, by $(E^{+\nu}_{\mathbf{k}+})^2(E^{-\nu}_{\mathbf{k}+})^2 =$

$[-h_0^2+(h_z+\nu h_t)^2+d_x^2]^2+4\Delta_A^2 d_x^2$, we see that nodal rings appear when $d_x=0$ and $(h_z+\nu h_t)^2=h_0^2$. This leads to the existence of rings in the $k_x=0$ plane when $-2t_1+h_0<h_z<2t_2+h_0$ or $-2t_1-h_0<h_z<2t_2-h_0$ or $-2t_2+h_0<h_z<2t_1+h_0$ or $-2t_2-h_0<h_z<2t_1-h_0$, if NNN hoppings are not involved. For the Weyl rings ($h_z\neq 0$), their number equals to the number of the above relations satisfied. The rings in other planes are associated with those in the $k_x=0$ plane by reciprocal vectors. The above conditions allow at most two Weyl rings when $h_0>2(t_y+t_z)$. We note that without h_z, the rings are Dirac rings, which split into Weyl rings when h_z is turned on. We also note that NNN hoppings only slightly modify the shape of nodal rings.

In Fig. 2(a), we plot the order parameter Δ_A in the (μ,h_z) plane, obtained by solving the nonlinear gap equations at zero temperature. As we have discussed, there exist two superfluid phases: SF1 and SF2. We can understand these two phases in two limits. In the first limit, we assume $t_{SO}=0$ and clearly $\Delta_A=\Delta_B$ as A and B sublattices can now be connected by a translational transformation. In the transformed model (4), the momenta of Cooper pairs equal to $(\pi/a_x,\pi/a_y,\pi/a_z)$ because of the band inversion [59]. We note that in the transformed model, SF1 and SF2 are associated with the order parameter $\Delta_j=(-1)^{j_x+j_y+j_z}\Delta_A$ and $\Delta_j=\Delta_A$, respectively. In the second limit, we assume $t_\nu=t_{N\nu}=0$, and in the transformed model, the momenta of Cooper pairs are zero, meaning that $\Delta_B=-\Delta_A$ in the original model. Although these two states can be simultaneously the energy minimum states as shown in Fig. 2(c) and (d), the ground state should be the one with the lower energy. Therefore with the change of parameters, these two phases can transition from one to another as shown in Fig. 2(b), where the ground state changes from SF1 to SF2 with increasing h_z. Clearly, this phase transition is the first order.

By examining the quasiparticle spectrum, we find that the SF1 phase is gapless only in a small region (the left part of the black line), whereas the SF2 phase is gapless in the whole region. In Fig. 2(e) and (f), we plot the gap (i.e., $\min(|E_{\mathbf{k}\gamma}|)$) of the quasiparticle spectrum in the $k_x=0$ plane for the parameters associated with the green and yellow squares in Fig. 2(a), displaying four and three Weyl rings, respectively. Similar to the nodal rings in the single-particle spectrum, the number of rings can be tuned by the Zeeman field or chemical potential.

Since both SF1 and SF2 phases have the chiral symmetry (i.e., $\mathcal{C}^{-1}H_{BdG}\mathcal{C}=-H_{BdG}$ with $\mathcal{C}=\sigma_x\tau_{N,y}$), similar to the single-particle case, we can associate a winding number n_w to any 1D closed path enclosing a Weyl ring [55],

$$n_w=\frac{1}{2\pi i}\int_{\theta=-\pi}^{\theta=\pi}d\theta\frac{d}{d\theta}\log\det A(\theta), \tag{6}$$

where $A(\theta)=H_0+i\Delta_A\sigma_y$ for the SF1 phase and $A(\theta)=H_0-i\Delta_A\tau_y\otimes\sigma_y$ for the SF2 phase, with $H_0=-(h_t\tau_x+\tilde{\mu})+d_x\tau_z\otimes\sigma_x+h_z\sigma_z$ and $k_\nu=k_\nu(\theta)$ referring to a 1D closed path. We find $n_w=\pm1$ for Weyl rings and the associated Berry phase is $\pm\pi$. In the SF1 phase, when $h_z=0$, there exist Dirac rings, which can be characterized by the winding number in the two subspaces with different eigenvalues $\sigma_y=\pm1$.

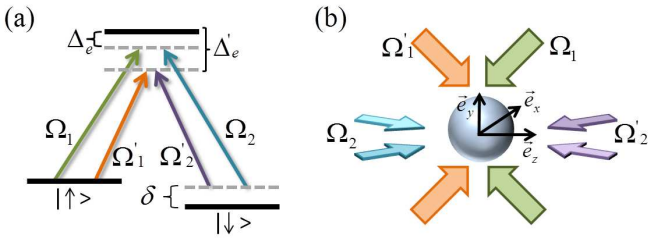

FIG. 3. (Color online) Schematics of a laser configuration to realize the Hamiltonian (1). Ω_1 and Ω_2, Ω_1' and Ω_2' are two sets of Raman laser beams coupling two hyperfine states $|\uparrow\rangle$ and $|\downarrow\rangle$. Δ_e and Δ_e' are the detunings, and δ is the two-photon detuning. Each Raman laser beam consists of two plane wave laser beams as shown in (b). These Raman laser beams also generate optical lattices via the Stark effects. Additional laser beams are also employed to create optical lattices along x and z.

Realization of nodal ring lattices: We propose an experimental setup (shown in Fig. 3) based on Raman coupling scheme for generating spin-orbit coupling [36, 47–52] to engineer the Hamiltonian (1).

Two independent pairs of red-detuned Raman lasers are used to couple two hyperfine states, such as $|\uparrow\rangle=|F=9/2,m_F=9/2\rangle$ and $|\downarrow\rangle=|F=9/2,m_F=7/2\rangle$ for ^{40}K atoms. One pair corresponds to the laser beams Ω_1 and Ω_2 with the Rabi frequencies $\Omega_1=\Omega_{10}\cos(k_{Ry}y)e^{-ik_{Rz}z/2}$ and $\Omega_2=i\Omega_{20}\sin(k_{Rx}x)e^{ik_{Rz}z/2}$, each of which can be generated by two plane wave laser beams. The other pair of Raman laser beams have the Rabi frequencies $\Omega_1'=\Omega_{10}'\cos(k_{Ry}y)e^{ik_{Rz}z/2}$ and $\Omega_2'=i\Omega_{20}'\sin(k_{Rx}x)e^{-ik_{Rz}z/2}$, respectively. The detunings $\Delta_e\gg\Omega=|\Omega_{10}\Omega_{20}|/\Delta_e$ and $\Delta_e'\gg\Omega'=|\Omega_{10}'\Omega_{20}'|/\Delta_e'$ to neglect the population in the excited states by the Raman procedure. The independence of two Raman coupling pairs are satisfied by $|\Delta_e-\Delta_e'|\gg\Omega,\Omega'$. These requirements are naturally satisfied in experiments (see the specific parameters in a typical experiment). Such two sets of Raman laser beams give rise to the spin-dependent lattice with $\Omega_{SO}=2\Omega$ and $k_{L\nu}=k_{R\nu}$ in Eq. (1) when $\Omega=\Omega'$, achieved when the two sets of Raman lasers come from the same resource. These laser beams also lead to optical lattices along the x and y directions via the stark effects: $-\delta V_x\sin^2(k_{Rx}x)$ and $-V_y\cos^2(k_{Ry}y)$ with $\delta V_x=(|\Omega_{20}|^2+|\Omega_{20}'|^2)/\Delta_e$ and $V_y=(|\Omega_{10}|^2+|\Omega_{10}'|^2)/\Delta_e$ (we have assumed $\Delta_e\approx\Delta_e'>0$ given that Δ_e and Δ_e' are both in the order of THz whereas $|\Delta_e-\Delta_e|'$ in the order of 10-100MHz). Moreover, one needs another stronger

optical lattices along the x direction: $-V_x'\cos^2(k_{Rx}x)$ with $V_x'>0$ so that the total x direction optical lattice is $-V_x\cos^2(k_{Rx}x)$ with $V_x=V_x'-\delta V_x>0$. Similarly, optical lattices along z, $-V_z\cos^2(k_{Rz}z)$ with $V_z>0$, can be generated. We note that the Raman laser beams can also create the Zeeman field $h_z=\delta/2$ with δ being the two-photon detuning.

In experiments, we consider ^{40}K atoms and choose $\Delta_e=2\pi\times1.46$THz that can be realized by a red-detuned laser beam with wavelength 773 nm [48], which gives the recoil energy $E_R/\hbar=2\pi\times8.3$kHz. A simple geometry of laser beams gives rise to $k_{Rx}=k_{Ry}=k_{Rz}=\sqrt{4/5}k_R$. The two pairs of Raman laser beams are independent as $|\Delta_e-\Delta_e'|\sim2\pi\times(10-100)$MHz $\gg E_R$. For $\Omega_{10}=\Omega_{10}'=2\pi\times0.14$ GHz and $\Omega_{20}=\Omega_{20}'=2\pi\times0.035$ GHz, we have $\Omega_{SO}=0.8E_R$, $V_y=3.2E_R$, and $\delta V_x=V_y/16$. For $\Omega_{3x}=\Omega_{3z}=2\pi\times0.21$ GHz, we have $V_x'=V_z=V_y$. δ can be readily tuned from zero. With these parameters, in the tight-binding model, $t=0.068E_R$, $t_x=1.17t$, $t_y=t_z=t$, $t_{N\nu}=t_N=-0.07t$, and $t_{SO}=0.53t$. The Dirac and Weyl rings in the single particle spectrum can be detected through the spin-resolved radio-frequency spectroscopy, similar to that in spin-orbit coupled atomic gases [36, 48, 49]. The rings in the superfluids may be detected by measuring the spectral density [38, 44] using the momentum resolved photoemission spectroscopy [60]. In terms of a BEC loaded in nodal ring lattices, one can measure Landau-Zener tunneling probability to detect the rings [35, 46] and the interference between two BECs traveling across a Weyl ring to extract the Berry phase [61].

Discussion: Not only nodal rings in 3D can be realized in the proposed experimental setup, but also Dirac cones in 2D can be engineered in a much simpler setup with only a pair of Raman laser beams (see supplementary information). In contrast to 2D Dirac cones in honeycomb lattices in previous experiments [35], there are two types of Dirac cones: one with four-fold degeneracies (each with Berry phase being π or $-\pi$ in the subspaces with $\sigma_y=\pm1$ similar to the 3D case) and one with two-fold degeneracies (each with Berry phase being π or $-\pi$). Without Zeeman fields, the former can exist, while with Zeeman fields, the former splits into two Dirac cones with two-fold degeneracies in separated positions in the momentum space. Such Dirac cones can be readily created, moved, and merged by tuning the lattice strength and Zeeman fields. Note that in previous experiments [35], the Dirac cones are formed due to the honeycomb lattice structure and the spin Zeeman field only shifts the relative energy between two Dirac cones for different spins, not their positions in the momentum space. In our model, the Zeeman field can split a four-fold degenerate Dirac cone into two located at different positions in the momentum space (see supplementary information).

In summary, we propose an experimental setup to engineer an optical lattice system that support nodal rings (i.e., Dirac or Weyl rings) in its single-particle spectrum. We study the superfluidity of Fermi gases with attractive interactions in such a lattice and show that the quasiparticle spectrum can also exhibit the nodal rings. Our scheme is based on previously already successful experimental setup and should pave the way for the experimental generation and observation of topological gapless materials.

Methods

BdG equation in momentum space: Here we only consider the BCS pairing with zero center-of-mass momenta Cooper pairs and hence Δ_A and Δ_B are spatially uniform. With a global $U(1)$ gauge invariance, although we can choose positive Δ_A and complex Δ_B for a general case, our numerical calculation shows that being real of Δ_B is energetically preferred. Therefore, with real Δ_B, $H_{\rm BCS}=\tau_{N,x}\otimes(\Delta_A\tau_z^+ + \Delta_B\tau_z^-)$ with $\tau_z^\pm=(\tau_0\pm\tau_z)/2$. The thermodynamical potential per site at the temperature $T=1/(k_B\beta)$ with Boltzmann constant k_B is

$$\Omega=\frac{1}{U}|\Delta_0|^2-\sum_{\mathbf{k}}\left[2\mu+\frac{1}{\beta}\sum_\gamma\frac{1}{2}\ln(1+e^{-\lambda\beta E_{\mathbf{k}\gamma}})\right], \quad (7)$$

with $\Delta_0^2=\Delta_A^2+\Delta_B^2$ and $E_{\mathbf{k}\gamma}$ with $\gamma=1,2,\cdots,8$ being the eigenvalues of $H_{\rm BdG}$. To obtain the mean-field order parameters, we solve the nonlinear gap equations

$$\partial\Omega/\partial\Delta_A=0,\ \partial\Omega/\partial\Delta_B=0. \quad (8)$$

For SF1 and SF2 phases, the pseudo-time-reversal symmetries correspond to $\mathcal{T}_1^{-1}H_{\rm BdG}\mathcal{T}_1=H_{\rm BdG}(-\mathbf{k})$ and $\mathcal{T}_2^{-1}H_{\rm BdG}\mathcal{T}_2=H_{\rm BdG}(-\mathbf{k})$ with $\mathcal{T}_1=\tau_{N,0}\otimes\mathcal{T}$ ($\tau_{N,0}$ is a 2×2 identity matrix) and $\mathcal{T}_2=\tau_{N,z}\otimes\mathcal{T}$, respectively. The inversion symmetries correspond to $\mathcal{I}_1^{-1}H_{\rm BdG}\mathcal{I}_1=H_{\rm BdG}(-\mathbf{k})$ and $\mathcal{I}_2^{-1}H_{\rm BdG}\mathcal{I}_2=H_{\rm BdG}(-\mathbf{k})$ with $\mathcal{I}_1=\tau_{N,0}\otimes\mathcal{I}$ and $\mathcal{I}_2=\tau_{N,z}\otimes\mathcal{I}$, respectively. The particle-hole symmetry is associated with the transformation $\Xi_j^{-1}H\Xi_j=-H(-\mathbf{k})$ ($j=1,2$) with $\Xi_1=i\tau_{N,y}\otimes\tau_x\otimes\sigma_y\mathcal{K}$ and $\Xi_2=i\tau_{N,x}\otimes\tau_x\otimes\sigma_y\mathcal{K}$ for SF1 and SF2, respectively.

* chuanwei.zhang@utdallas.edu

[1] G. E. Volovik, The Universe in a Helium Droplet (Clarendon Press, Oxford, 2003).

[2] A. H. Castro Neto, F. Guinea, N. M. R. Peres, K. S. Novoselov, and A. K. Geim, The electronic properties of graphene. Rev. Mod. Phys. **81,** 109 (2009).

[3] M. Z. Hasan and C. L. Kane Topological insulators. Rev. Mod. Phys. **82,** 3045 (2010).

[4] X.-L. Qi and S.-C. Zhang, Topological insulators and superconductors. Rev. Mod. Phys. **83,** 1057 (2011).

[5] S. M. Young *et al.* Dirac Semimetal in Three Dimensions. Phys. Rev. Lett. **108,** 140405 (2012).

[6] X. Wan, A. M. Turner, A. Vishwanath, and S. Y. Savrasov, Topological semimetal and Fermi-arc surface

states in the electronic structure of pyrochlore iridates. Phys. Rev. B **83,** 205101 (2011).
[7] K.-Y. Yang, Y.-M. Lu, and Y. Ran, Quantum Hall effects in a Weyl semimetal: Possible application in pyrochlore iridates. Phys. Rev. B **84,** 075129 (2011).
[8] A. A. Burkov and L. Balents, Weyl semimetal in a topological insulator multilayer. Phys. Rev. Lett. **107,** 127205 (2011).
[9] G. Xu, H. Weng, Z. Wang, X. Dai, and Z. Fang, Chern semimetal and the quantized anomalous Hall effect in $HgCr_2Se_4$. Phys. Rev. Lett. **107,** 186806 (2011).
[10] L. Lu, L. Fu, J. D. Joannopoulos, and M. Soljačić, Weyl points and line nodes in gapless gyroid photonic crystals. Nature photonics **7,** 294 (2013).
[11] H. Weng, C. Fang, Z. Fang, A. Bernevig, and X. Dai, Weyl semimetal phase in noncentrosymmetric transition-metal monophosphides. Phys. Rev. X **5,** 011029 (2015).
[12] S.-M. Huang *et al.*, A Weyl fermion semimetal with surface Fermi arcs in the transition metal monopnictide TaAs class. Nature Commun. **6,** 7373 (2015).
[13] M. Neupane *et al.*, Observation of a topological 3D Dirac semimetal phase in high-mobility Cd3As2 and related materials. Nature Commun. **05,** 3786 (2014).
[14] S. Borisenko *et al.*, Experimental Realization of a Three-Dimensional Dirac Semimetal. Phys. Rev. Lett. **113,** 027603 (2014).
[15] Z. K. Liu *et al.*, Discovery of a Three-dimensional Topological Dirac Semimetal, Na3Bi. Science **343,** 864 (2014).
[16] L. Lu *et al.*, Experimental observation of Weyl points arXiv:1502.03438 (2015).
[17] X.-Y. Xu *et al.*, Experimental realization of a topological Weyl semimetal phase with Fermi arc surface states in TaAs arXiv:1502.03807 (2015).
[18] B. Q. Lv *et al.*, Discovery of Weyl semimetal TaAs arXiv:1502.04684 (2015).
[19] A. A. Burkov, M. D. Hook, and L. Balents, Topological nodal semimetals, Phys. Rev. B **84,** 235126 (2011).
[20] J.-M. Carter, V. V. Shankar, M. A. Zeb, and H.-Y. Kee, Semimetal and Topological Insulator in Perovskite Iridates, Phys. Rev. B **85,** 115105 (2012).
[21] Y. Chen, Y.-M. Lu, and H.-Y. Kee, Topological crystalline metal in orthorhombic perovskite iridates, Nature Communications **6,** 6593 (2015).
[22] R. Schaer, E. K. H. Lee, Y.-M. Lu, and Y. B. Kim, Topological Spinon Semimetals and Gapless Boundary States in Three Dimensions, Phys. Rev. Lett. **114,** 116803 (2015).
[23] Y. Chen *et al.*, Spin-orbit-free Weyl-loop and Weyl-point semimetals in a stable three-dimensional carbon allotrope arXiv:1505.02284 (2015).
[24] Y. Kim, B. J. Wieder, C. L. Kane, and A. M. Rappe, Dirac Line Nodes in Inversion Symmetric Crystals arXiv:1504.03807 (2015).
[25] L. S. Xie, L. M. Schoop, E. M. Seibel, Q. D. Gibson, W. Xie, and R. J. Cava, Potential ring of Dirac nodes in a new polymorph of Ca3P2, APL Mat. **3,** 083602 (2015).
[26] M. Zeng *et al.*, Topological semimetals and topological insulators in rare earth monopnictides arXiv:1504.03492 (2015).
[27] R. Yu, H. Weng, Z. Fang, X. Dai, and X. Hu, Topological Nodal Line Semimetal and Dirac Semimetal State in Antiperovskite Cu3PdN, Phys. Rev. Lett. **115,** 036807 (2015).
[28] G. Bian, *et al.* Topological nodal-line fermions in the noncentrosymmetric superconductor compound PbTaSe2, arXiv:1505.03069.
[29] N. B. Kopnin, T. T. Heikkilä, and G. E. Volovik, High-temperature surface superconductivity in topological flat-band systems, Phys. Rev. B **83,** 220503 (2011).
[30] G. Jotzu *et al.*, Experimental realisation of the topological Haldane model, Nature **515,** 237 (2014).
[31] M. Atala *et al.*, Direct measurement of the Zak phase in topological Bloch bands, Nature Physics **9,** 795 (2013).
[32] M. Lohse *et al.*, A Thouless Quantum Pump with Ultracold Bosonic Atoms in an Optical Superlattice arXiv:1507.02225 (2015).
[33] S. Nakajima *et al.*, Topological Thouless Pumping of Ultracold Fermions, arXiv:1507.02223 (2015).
[34] H.-I. Lu, M. Schemmer, L.M. Aycock, D. Genkina, S. Sugawa, and I.B. Spielman, Geometrical pumping with a Bose-Einstein condensate, arXiv:1508.04480.
[35] L. Tarruell *et al.*, Creating, moving and merging Dirac points with a Fermi gas in a tunable honeycomb lattice, Nature **483,** 302 (2012).
[36] L. Huang *et al.*, Experimental realization of a two-dimensional synthetic spin-orbit coupling in ultracold Fermi gases arXiv:1506.02861 (2015).
[37] M. Gong, S. Tewari, and C. Zhang, BCS-BEC crossover and topological phase transition in 3D spin-orbit coupled degenerate Fermi gases. Phys. Rev. Lett. **107,** 195303 (2011).
[38] K. Seo, L. Han, and C. A. R. Sá de Melo, Emergence of Majorana and Dirac particles in ultracold fermions via tunable interactions, spin-orbit effects, and Zeeman fields. Phys. Rev. Lett.**109,** 105303 (2012).
[39] T. Das, Weyl semimetal and superconductor designed in an orbital-selective superlattice. Phys. Rev. B **88,** 035444 (2013).
[40] K. Seo, C. Zhang, and S. Tewari, Thermodynamic signatures for topological phase transitions to Majorana and Weyl superfluids in ultracold Fermi gases. Phys. Rev. A **87,** 063618 (2013).
[41] Y. Xu, R.-L. Chu, and C. Zhang, Anisotropic Weyl fermions from the quasiparticle excitation spectrum of a 3D Fulde-Ferrell superfluid. Phys. Rev. Lett. **112,** 136402, (2014).
[42] H. Hu, L. Dong, Y. Cao, H. Pu, and X.-J. Liu, Gapless topological Fulde-Ferrell superfluidity induced by an in-plane Zeeman field. Phys. Rev. A **90,** 033624 (2014).
[43] B. Liu, X. Li, L. Yin, and W. V. Liu, Weyl superfluidity in a three-dimensional dipolar Fermi gas. Phys. Rev. Lett. **114,** 045302 (2015).
[44] Y. Xu, F. Zhang, and C. Zhang, Structured Weyl Points in Fulde-Ferrell Superfluids arXiv:1411.7316 (2015).
[45] T. Dubček, *et al.* Weyl points in three-dimensional optical lattices: synthetic magnetic monopoles in momentum space, Phys. Rev. Lett. **114,** 225301 (2015).
[46] W.-Y. He, S. Zhang, and K. T. Law, The Realization and Dectection of Weyl Semimetals in Cold Atomic Systems arXiv:1501.02348 (2015).
[47] Y. -J. Lin, K. Jiménez-García, and I. B. Spielman, Spin-orbit-coupled Bose-Einstein condensates. Nature **471,** 83 (2011).
[48] P. Wang *et al.*, Spin-orbit coupled degenerate Fermi gases. Phys. Rev. Lett. **109,** 095301 (2012).
[49] L. W. Cheuk *et al.*, Spin-injection spectroscopy of a spin-orbit coupled Fermi gas. Phys. Rev. Lett. **109,** 095302 (2012).

[50] J. -Y. Zhang *et al.*, Collective dipole oscillations of a spin-orbit coupled Bose-Einstein condensate. Phys. Rev. Lett. **109,** 115301 (2012).
[51] C. Qu, C. Hamner, M. Gong, C. Zhang, and P. Engels, Observation of Zitterbewegung in a spin-orbit-coupled Bose-Einstein condensate. Phys. Rev. A **88,** 021604(R) (2013).
[52] R. A. Williams, M. C. Beeler, L. J. LeBlanc, K. Jiménez-García, and I. B. Spielman, Raman-induced interactions in a single-component Fermi gas near an s-wave Feshbach resonance. Phys. Rev. Lett. **111,** 095301 (2013).
[53] This pseudo-time-reversal symmetry corresponds to the symmetry in the continous model defined by $\Pi^{-1}H\Pi = H$ with $\Pi = i\sigma_y\mathcal{K}\mathcal{P}$ and $\mathcal{P}^{-1}H\mathcal{P} = H(-x)$.
[54] X.-J. Liu, K. T. Law, and T. K. Ng, Realization of 2D Spin-Orbit Interaction and Exotic Topological Orders in Cold Atoms, Phys. Rev. Lett. **112,** 086401 (2014).
[55] S. Tewari and J. D. Sau, Topological Invariants for Spin-Orbit Coupled Superconductor Nanowires, Phys. Rev. Lett. **109**, 150408 (2012).
[56] D. Xiao, M.-C. Chang, and Q. Niu, Berry phase effects on electronic properties, Rev. Mod. Phys. **82,** 1959 (2010).
[57] F. Zhang, C. L. Kane, and E. J. Mele, Topological Mirror Superconductivity, Phys. Rev. Lett. **111**, 056403 (2013).
[58] S. A. Yang, H. Pan, and F. Zhang, Dirac and Weyl Superconductors in Three Dimensions, Phys. Rev. Lett. **113,** 046401 (2014).
[59] Z. Zheng, C. Qu, X. Zou, and C. Zhang, Fulde-Ferrell superfluids without spin-imbalance in three-dimensional driven spinful fermionic optical lattices arXiv:1501.00448 (2015).
[60] J. T. Stewart, J. P. Gaebler, and D. S. Jin, Using photoemission spectroscopy to probe a strongly interacting Fermi gas, Nature **454**, 744 (2008).
[61] L. Duca, T. Li, M. Reitter, I. Bloch, M. Schleier-Smith, and U. Schneider, An Aharonov-Bohm interferometer for determining Bloch band topology, Science **347**, 288 (2015).

Acknowledgements: We would like to thank P. Engels, F. Zhang, and C. Liu for helpful discussions. Y.X. and C.Z are supported by ARO (W911NF-12-1-0334), AFOSR (FA9550-13-1-0045), and NSF (PHY-1505496). We also thank Texas Advanced Computing Center, where part of our numerical calculations was performed.

Author contributions All authors took part in the discussing of the results, designing of the experiment setup, and the writing of the manuscript. Y. Xu conceived the idea and obtained the numerical results. C. Zhang supervised the project.

Competing financial interests

The authors declare no competing financial interests.

S-1. DERIVATION OF TIGHT-BINDING MODEL

In this supplementary material, we derive the tight-binding model from the continuous model (1) in the main text and compare the single-particle spectra of the tight-binding and continuous models for typical parameters in experiments.

In the second quantization representation, the Hamiltonian takes the form

$$H_{II} = \int d\mathbf{r}\hat{\psi}^\dagger(\mathbf{r})H\hat{\psi}(\mathbf{r}), \tag{S1}$$

where H is the single-particle Hamiltonian in Eq.(1) in the main text, $\hat{\psi}(\mathbf{r}) = (\ \hat{\psi}_\uparrow(\mathbf{r})\ \ \hat{\psi}_\downarrow(\mathbf{r})\ )^T$ where $\hat{\psi}_\sigma(\mathbf{r})$ $[\hat{\psi}^\dagger_\sigma(\mathbf{r})]$ annihilates (creates) an atom with spin σ ($\sigma =\uparrow,\downarrow$) located at $\mathbf{r}$. They satisfy the anti-commutation or commutation relation $[\hat{\psi}_\sigma(\mathbf{r}), \hat{\psi}^\dagger_{\sigma'}(\mathbf{r}')]_\pm = \delta_{\sigma\sigma'}\delta(\mathbf{r}-\mathbf{r}')$ for fermionic atoms (+) or bosonic atoms (−), respectively. The field operator can be expanded by local Wannier functions

$$\hat{\psi}_\sigma(\mathbf{r}) = \sum_{nj\sigma} W_{nj\sigma}\hat{c}_{n,j,\sigma}, \tag{S2}$$

where $W_{nj\sigma}$ is the Wannier function located at the j-th site for the n-th band for spin σ, and $\hat{c}_{n,j,\sigma}$ annihilates an atom at the j-th site in the n-th band with spin σ. As we only consider the physics in the lowest band, let us assume $n = 1$ and further assume that the Wannier function $W_{1j\sigma}$ can be approximated by the lowest band Wannier function W_j of the Hamiltonian with pure spin-independent optical lattices. Hence

$$\hat{\psi}_\sigma(\mathbf{r}) \approx \sum_j W_j\hat{c}_{j,\sigma}, \tag{S3}$$

where $W_j = W^x_{j_x}(r_x)W^y_{j_y}(r_y)W^z_{j_z}(r_z)$ with $W^\nu_{j_\nu}(r_\nu) = W^\nu(r_\nu - j_\nu a_\nu)$ being the Wannier function along ν. Based on this expansion, the tight-binding model without H_{SO} reads

$$H_1 = -\sum_j\sum_\sigma\sum_\nu(t_\nu\hat{c}^\dagger_{j,\sigma}\hat{c}_{j_\nu+1,\sigma} + t_{N\nu}\hat{c}^\dagger_{j,\sigma}\hat{c}_{j_\nu+2,\sigma} + h.c.) + h_z\sum_j(\hat{c}^\dagger_{j,\uparrow}\hat{c}_{j,\uparrow} - \hat{c}^\dagger_{j,\downarrow}\hat{c}_{j,\downarrow}) \tag{S4}$$

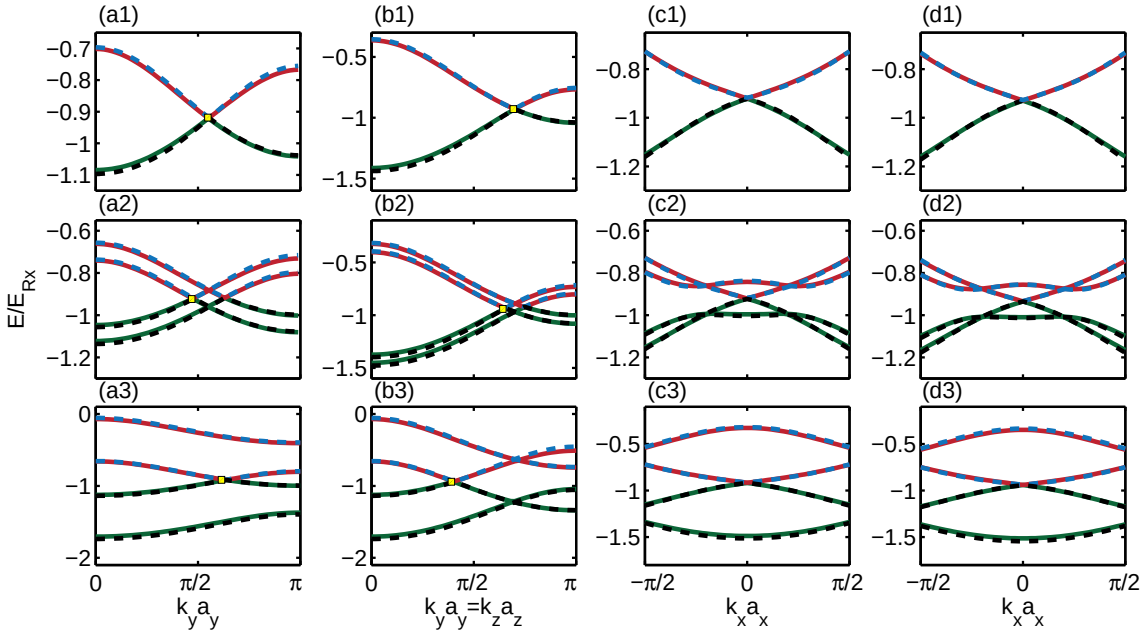

FIG. S1. (Color online) Single-particle spectra obtained by the tight-binding model (dashed blue and black lines) and the continuous model (solid red and green lines). Each row panel from top to bottom is associated with $h_z = 0$, $h_z = 0.032E_R$, and $h_z = 0.24E_R$, respectively. The first and second column panels (from left to right) correspond to $(k_x = 0, k_z a_z = \pi)$ and $(k_x = 0)$, respectively. The third and fourth column panels plot the spectra along k_x around touching points (yellow squares) corresponding to the first and second column panels, respectively. The parameters for the continuous model are $k_{Lx} = k_{Ly} = k_{Lz} = \sqrt{4/5}k_R$, $V_x = V_y = V_z = 3.2E_R$, and $\Omega_{SO} = 0.8E_R$; the parameters for the tight-binding model are $t = t_y = t_z = 0.068E_R$ and $t_N = -0.07t$ and $t_{SO} = 0.53t$. The recoil energy along x is $E_{Rx} = \hbar^2 k_{Lx}^2/2m = 0.8E_R$.

with the inclusion of the nearest and next nearest neighbor hopping with the corresponding hopping amplitudes being

$$t_\nu = -\int dr_\nu W_j \left[\frac{p_\nu^2}{2m} - V_\nu \cos^2(k_{L\nu} r_\nu)\right] W_{j_\nu+1}, \tag{S5}$$

$$t_{N\nu} = -\int dr_\nu W_j \left[\frac{p_\nu^2}{2m} - V_\nu \cos^2(k_{L\nu} r_\nu)\right] W_{j_\nu+2}. \tag{S6}$$

The tight-binding term contributed by the spin-dependent lattices can be derived as follows

$$H_{SO} = i\Omega_{SO} \int d\mathbf{r} \hat{\psi}_\uparrow^\dagger(\mathbf{r}) V_{SO} \hat{\psi}_\downarrow(\mathbf{r}) + h.c. \tag{S7}$$

$$\approx i\Omega_{SO} \sum_{j,j'} \hat{c}_{j,\uparrow}^\dagger \hat{c}_{j',\downarrow} t_{SO}^{jj'} + h.c., \tag{S8}$$

where

$$t_{SO}^{jj'} = \int d\mathbf{r} W_j V_{SO} W_{j'} = \prod_{\nu=x,y,z} t_{SO}^{j_\nu j'_\nu},$$

with

$$t_{SO}^{j_x j'_x} = t_{SO}^{j'_x j_x} = \int dr_x W_{j_x}^x(r_x) \sin(k_{Lx} r_x) W_{j'_x}^x(r_x), \tag{S9}$$

$$t_{SO}^{j_y j'_y} = t_{SO}^{j'_y j_y} = \int dr_y W_{j_y}^y(r_y) \cos(k_{Ly} r_y) W_{j'_y}^y(r_y), \tag{S10}$$

$$t_{SO}^{j_z j'_z} = t_{SO}^{j'_z j_z} = \int dr_z W_{j_z}^z(r_z) \cos(k_{Lz} r_z) W_{j'_z}^z(r_z). \tag{S11}$$

Because one of the optical wells is located at $\mathbf{r} = (0, 0, 0)$, $W_0^\nu(r_\nu) = W_0^\nu(-r_\nu)$ and

$$t_{SO}^{j_x j_x} = t_{SO}^{j_x j_x+2} = t_{SO}^{j_y j_y+1} = t_{SO}^{j_z j_z+1} = 0, \tag{S12}$$

$$t_{SO}^{j_\nu j_\nu+1} = -t_{SO}^{j_\nu+1 j_\nu+2}, \tag{S13}$$

$$t_{SO}^{j_\nu j_\nu} = -t_{SO}^{j_\nu+1 j_\nu+1}, \tag{S14}$$

where the last two relations are obtained because the period of the spin-independent optical lattices is a half of that of the spin-dependent ones along each direction. Therefore, with the nearest-neighbor hopping (no next nearest-neighbor hopping exists), the position dependent spin-orbit coupling term of the tight-binding model reads

$$H_{SO} = i\Omega_{SO} \sum_j \left[\hat{c}_{j,\uparrow}^\dagger \hat{c}_{j_x+1,\downarrow} t_{SO}^{j_x j_x+1} t_{SO}^{j_y j_y} t_{SO}^{j_z j_z} + \hat{c}_{j,\uparrow}^\dagger \hat{c}_{j_x-1,\downarrow} t_{SO}^{j_x j_x-1} t_{SO}^{j_y j_y} t_{SO}^{j_z j_z}\right] + h.c. \tag{S15}$$

$$= i\Omega_{SO} \sum_j \left[\hat{c}_{j,\uparrow}^\dagger \hat{c}_{j_x+1,\downarrow} - \hat{c}_{j,\uparrow}^\dagger \hat{c}_{j_x-1,\downarrow}\right] t_{SO}^{j_x j_x+1} t_{SO}^{j_y j_y} t_{SO}^{j_z j_z} + h.c. \tag{S16}$$

$$= it_{SO} \sum_j (-1)^{j_x+j_y+j_z} \left[\hat{c}_{j,\uparrow}^\dagger \hat{c}_{j_x+1,\downarrow} - \hat{c}_{j,\uparrow}^\dagger \hat{c}_{j_x-1,\downarrow}\right] + h.c. \tag{S17}$$

where

$$t_{SO} = \Omega_{SO} t_{SO}^{01} t_{SO}^{00} t_{SO}^{00}. \tag{S18}$$

Therefore, we obtain the tight-binding model in Eq.(2) in the main text ($H_1 = H_h + H_Z$).

We now consider a specific set of experimental parameters used in the main text, yielding $k_{Lx} = k_{Ly} = k_{Lz} = \sqrt{4/5}k_R$, $V_x = V_y = V_z = 3.2E_R$, and $\Omega_{SO} = 0.8E_R$. The tight-binding parameters are calculated from Eq. (S5), Eq. (S6), and Eq. (S18), yielding $t = t_y = t_z = 0.068E_R$, $t_N = -0.07t$, and $t_{SO} = 0.53t$. We note that we choose $t_x = 1.17t$, which is slightly different from t_y and t_z given the distinct correction of Wannier functions by V_{SO} along x. In Fig. S1, we compare the single-particle spectra obtained by the tight-binding model with that obtained by the continuous model, showing their good agreement with each other.

S-2. DIRAC CONES IN TWO DIMENSIONS

We consider a two-dimensional case with the following Hamiltonian

$$H_{2D} = \frac{\mathbf{p}^2}{2m} - \sum_{\nu=x,y} V_\nu \cos^2(k_R r_\nu) + h_z\sigma_z - V_{SO}\sigma_y, \tag{S19}$$

where $V_{SO} = \Omega_{SO} \sin(k_{L_R} r_x) \cos(k_{L_R} r_y)$. Compared with the experimental setup for the 3D scenario in Fig. 3 in the main text, the setup to realize this Hamiltonian is much easier. One only needs a pair of Raman laser beams [shown in Fig. S2 (a) and (b)] with Rabi frequencies $\Omega_1 = \Omega_{10} \cos(k_R y)$ and $\Omega_2 = i\Omega_{20} \sin(k_R x)$, and an additional standing laser beam to engineer an optical lattice along x. The tight-binding model of this Hamiltonian is a simplified version of Eq. (3) when the hopping terms along x and y are kept and

$$H_{SO} = it_{\rm SO} \sum_j (-1)^{j_x+j_y} (\hat{c}_{j,\uparrow}^\dagger \hat{c}_{j_x+1,\downarrow} - \hat{c}_{j,\uparrow}^\dagger \hat{c}_{j_x-1,\downarrow}) + h.c.. \tag{S20}$$

Clearly, the Hamiltonian in the momentum space is also a simplified version of the Hamiltonian (3) in the main text when only the hopping terms along x and y are kept. Dirac cones appear when $h_z + \lambda h_t = 0$ on the $k_x = 0$ line. Different from the 3D case, when $h_z = 0$, two Dirac cones [as displayed in Fig. S2(c)] with four-fold degeneracies (each with Berry phase being π or $-\pi$ in the subspaces with $\sigma_y = \pm 1$ similar to the 3D case) can appear only when $t_y > t_x$, which can be realized by choosing a stronger optical lattice along the x direction than that along the y direction. At the critical point $t_y = t_x$, the spectrum becomes quadratic along y and keeps linear along x. In the presence of h_z, each Dirac cone with four-fold degeneracies splits into two Dirac cones with two-fold degeneracies (each with Berry phase being π or $-\pi$) at different positions in the momentum space as shown in Fig. S2(d). They can exist as long as $2(t_x - t_y) < h_z < 2(t_y + t_x)$ and $-(t_x + t_y) < h_z < 2(t_y - t_x)$. When $h_z = \pm 2(t_x + t_y)$ and $h_z = \pm 2(t_y - t_x)$, two Dirac cones with two-fold degeneracies merge—with spectra being quadratic along y and linear along x—at $(k_x = 0, k_y = 0)$ and $(k_x = 0, k_y = \pi)$, respectively.

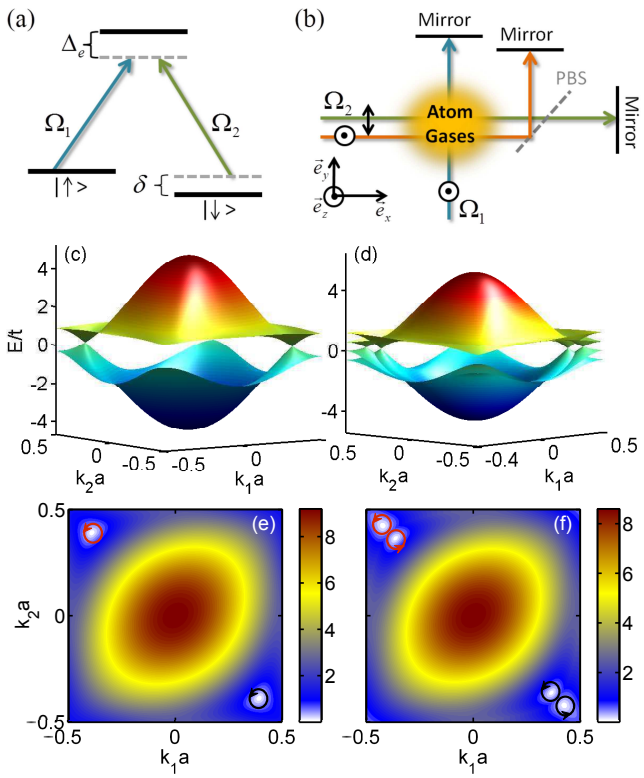

FIG. S2. (Color online) Schematics of a laser configuration to realize the 2D Hamiltonian with Dirac cones and the single-particle spectra of such optical lattice systems. Ω_1 and Ω_2 are two Raman laser beams coupling two hyperfine states $|\uparrow\rangle$ and $|\downarrow\rangle$. Δ_e is the detuning, and δ is the two-photon detuning. Each Raman laser beam is a standing wave formed by a plane wave laser beam reflected by a mirror as shown in (b). These Raman laser beams also generate optical lattices via the Stark effects. An additional laser beam (red line) with different frequency from the Raman lasers (shifted by ∼100MHz using an acoustic-optical modulator (AOM)) is also employed to create optical lattices along x. PBS denotes polarizing beamsplitter. Double arrow and circle dots denote the polarization direction of laser beams. The PBS separates the Raman beam and the optical lattice beams so that their phases can be controlled individually by different mirrors. (c)(d) Single-particle spectra of the tight-binding Hamiltonian without and with Zeeman fields, respectively. (e)(f) The gap distribution between particle and hole branches in the momentum space. The white points indicate the Dirac cones and the Berry phase calculated along the red circle (black one) is π $(-\pi)$. Note in (e) the Berry phase is calculated in the subspace of σ_y. Here $t_x = t$, $t_y = 1.3t$, $t_N = 0.07t$, and $t_{SO} = 0.64t$. The lattice constants are $a_x = a_y = a$ and the crystal momenta are $a\mathbf{k} = \pi(k_1 + k_2)\mathbf{e}_x + \pi(-k_1 + k_2)\mathbf{e}_y$.